

Supporting Information for:

Slab Rollback Orogeny model: A test-of-concept

Luca Dal Zilio^{1,2*}, Edi Kissling¹, Taras Gerya¹, and Ylona van Dinther^{1,3}

¹ Department of Earth Sciences, ETH Zürich, Sonneggstrasse 5, 8092 Zürich, Switzerland

² Seismological Laboratory, California Institute of Technology, 1200 E California Blvd, Pasadena, USA

³ Department of Earth Sciences, Utrecht University, Princetonlaan 8A/4, Utrecht, Netherlands

Contents of this file

1. Supplementary text
2. Tables S1 and S2
3. Figures S1 to S15
4. Movie S1
5. Supporting References

1. Initial model design

1.1. Numerical code description

In order to simulate the dynamics of mountain building processes coupled to mantle dynamics, we employ the seismo-thermo-mechanical (STM) (van Dinther et al., 2013). This numerical code solves for the two-dimensional steady state momentum equations and heat conservation equation using the finite-difference/marker-in-cell method on a Eulerian grid (Gerya & Yuen, 2007):

$$\frac{\partial v_x}{\partial x} + \frac{\partial v_z}{\partial z} = 0 ; \quad (1)$$

$$\frac{\partial \sigma'_{xx}}{\partial x} + \frac{\partial \sigma'_{xz}}{\partial z} - \frac{\partial P}{\partial x} = \rho \frac{Dv_x}{Dt} ; \quad (2)$$

$$\frac{\partial \sigma'_{zz}}{\partial z} + \frac{\partial \sigma'_{zx}}{\partial x} - \frac{\partial P}{\partial z} = \rho \frac{Dv_z}{Dt} - \rho g . \quad (3)$$

These equations are solved to obtain the horizontal and vertical velocities (v_x and v_z) and pressure (P , defined as the mean stress), whereas ρ is density, σ'_{ij} are deviatoric stress tensor components, and $g = 9.81 \text{ m/s}^2$ is the vertical component of the gravitation acceleration. The advection of transport properties including viscosity, plastic strain and temperature is performed with the displacement of Lagrangian markers.

The momentum equations include the inertial term to stabilize higher slip rates at low time steps. A time step of 1 year, however, reduces our formulation to a virtually quasi-static one. Ruptures during the resulting events hence represent the occurrence of rapid threshold-exceeding slip during which permanent displacement and stress drop occur along a localized interface.

The heat equation describes the balance of heat in a continuous medium and is solved in a Lagrangian manner and is expressed in the following way (Gerya, 2010):

$$\rho C_p \frac{DT}{Dt} = - \frac{\partial q_x}{\partial x} - \frac{\partial q_z}{\partial z} + H_r + H_a + H_s ; \quad (4)$$

$$q_x = -k(T, C) \frac{\partial T}{\partial x}; \quad (5)$$

$$q_z = -k(T, C) \frac{\partial T}{\partial z}; \quad (6)$$

$$H_a = T \alpha \frac{DP}{Dt}; \quad (7)$$

$$H_s = \sigma'_{ij} \dot{\epsilon}_{ij, vp}. \quad (8)$$

This formulation takes into account the effect of radioactive heating (H_r), adiabatic heat production/consumption (H_a), and shear heating (H_s). DP/Dt represents the substantive time derivative of pressure, whereas α is the thermal expansion. Thermal conductivity $k(T, C)$ is a function of both temperature and composition (Table S1). q_x and q_z are the horizontal and vertical components of the heat flux vector, $\dot{\epsilon}_{ij, vp}$ is the visco-plastic component of the deviatoric strain rate tensor. The isobaric heat capacity (C_p) and isothermal compression term are computed at each timestep and takes into account the effect of latent heat due to phase transformations (Faccenda & Dal Zilio, 2017). Evaluation of H_T and H_s terms requires information from the pressure and stress tensor components. These terms are thus computed after solving the Stokes equations. The heat equation can then be solved taking into account the effect of isothermal compression, phases changes and shear heating at the current timestep.

1.2. Rheological model

We consider that the strength of the lithosphere is controlled, at the different timescales of orogeny, by the combination of both brittle and ductile deformation mechanisms in a visco-elasto-plastic rheology. Viscous creep is computed in terms of deformation invariants and depends on strain rate, temperature, and pressure (Ranalli, 1995). The effective viscosity (η_{eff}) of the deformation is calculated as a combination of diffusion (η_{diff}) and dislocation creep (η_{dis}):

$$\frac{1}{\eta_{eff}} = \frac{1}{\eta_{diff}} + \frac{1}{\eta_{disl}}. \quad (9)$$

The calculation of the viscosity associated with dislocation creep regime is formulated as follows:

$$\eta_{disl} = \frac{1}{2} A_d \sigma_{II}^{1-n} \exp\left(\frac{E_a + PV_a}{nRT}\right), \quad (10)$$

where σ_{II} is the second invariant of deviatoric stress tensor, A_d is the pre-exponential factor, E_a the activation energy, V_a is the activation volume, n the stress exponent, and R is the gas constant. Those material properties are determined from laboratory flow experiments and are given in Table S1.

Dislocation creep is dominant for high stress levels, while diffusion creep is a thermally activated mechanism and is the most convenient way to accommodate deformation at low stress conditions:

$$\eta_{diff} = \frac{1}{2} A_d \tau_{tr}^{1-n} \exp\left(\frac{E_a + PV_a}{nRT}\right). \quad (11)$$

In this case, τ_{tr} defines the stress transition between diffusion creep and dislocation creep, which is assumed to occur at 30 kPa (Turcotte & Schubert, 2002).

Our rheological model takes into account a second semi-brittle deformation mechanism characterized by the exponential flow of olivine and also known as Peierls mechanism. As demonstrated in Duretz et al. (2011), Peierls creep in olivine is a key mechanism for slab breakoff, generally causing slabs to break earlier and at shallower depths. This flow mechanism has been put in evidence in a number experimental studies (Evans & Goetze, 1979; Katayama & Karato, 2008). Moreover, recent studies have shown that the existence of plate tectonics requires sufficiently lithospheric yield stress that are lower than Mohr–Coulomb stresses (Van Heck & Tackley, 2008). Such conditions necessitate the use of stress limiters such as Peierls creep which promotes the localization of deformation in the lithospheric mantle (Kameyama et al., 1999; Lu et al., 2011). The effective viscosity corresponding to the Peierls creep regime is characterized

by an exponential dependance on the second stress invariant and is formulated as:

$$\eta_{peierls} = \frac{1}{2A_{peierls}\sigma_{II}} \exp\left(\frac{E_a + PV_a}{nRT} \left(1 - \left(\frac{\sigma_{II}}{\sigma_{peierls}}\right)^p\right)^q\right). \quad (12)$$

For dry olivine, $A_{peierls} = 10^{7.8} 10^{-12} Pa^{-2}s^{-1}$ is the material constant for Peierls creep, $\sigma_{peierls}$ is the Peierls stress that limits the strength of the material and corresponds to 9.1 GPa (Evans & Goetze, 1979). Exponents p and q depend on the shape and geometry of obstacles that limit the dislocation motion and are equal to 1 and 2, respectively. The Peierls mechanism is a dominant deformation mechanism of the downgoing slab, where the temperature is low and stress is high (Karato et al., 2001).

The 2-D steady state momentum equations are solved using constitutive relations that relate deviatoric stresses and strain rates in a nonlinear visco-elasto-plastic manner:

$$\varepsilon_{ij} = \frac{1}{2G} \frac{D\sigma'_{ij}}{Dt} + \frac{1}{2\eta} \sigma'_{ij} + \begin{cases} 0 & \text{for } \sigma'_{II} < \sigma_{yield} \\ \chi \frac{\partial \sigma'_{II}}{\partial \sigma'_{ij}} = \chi \frac{\partial \sigma'_{ij}}{\partial \sigma'_{II}} & \text{for } \sigma'_{II} = \sigma_{yield} \end{cases} \quad (13)$$

where G is shear modulus and η is effective viscosity. $D\sigma'_{ij}/Dt$ is the objective co-rotational time derivative solved using a time explicit scheme (Gerya, 2010) and $\sigma_{II} = \sqrt{\sigma'_{xx}{}^2 + \sigma'_{xz}{}^2}$ is the second invariant of the deviatoric stress tensor, and χ is a plastic multiplier connecting plastic strain rates and stresses. Introducing a visco-plastic viscosity (η_{vp}), we can rewrite eq. 13 as:

$$\sigma'_{ij} = 2\eta_{vp}Z\dot{\varepsilon}_{ij} + \sigma_{ij}(1 - Z) \quad (14)$$

where Z is the visco-elasticity factor:

$$Z = \frac{G\Delta t_{comp}}{G\Delta t_{comp} + \eta_{vp}} \quad (15)$$

where Δt_{comp} is the computational time step.

The brittle part of the lithosphere is controlled by Mohr–Coulomb (or non-associative Drucker-Prager) plasticity which expresses the linear dependence of the geomaterials resistance on the total pressure Prager and Drucker (1952). Mohr–Coulomb plasticity acts as a stress lim-

iter in the regions where the second stress invariant (σ_{ii}) exceeds the material yield stress. The yield stress depends on the pressure, the standard strength (i.e., cohesion) C , and the effective friction coefficient μ_{eff} :

$$\sigma_{yield} = C + \mu_{eff} P. \quad (16)$$

An important component in the yield criterion is the friction coefficient. Following the approach of van Dinther et al. (2013), we apply a strongly rate-dependent friction formulation (Ampuero & Ben-Zion, 2008), in which the effective friction coefficient μ_{eff} depends on the visco-plastic slip velocity $V = (\sigma_{yield}/\eta_m)\Delta x$, in which η_m is the local viscosity from the previous time step and Δx is the Eulerian grid size:

$$\mu_{eff} = \frac{V_c \mu_s + V \mu_d}{V_c + V} \quad (17)$$

$$\gamma = 1 - (\mu_d/\mu_s) \quad (18)$$

where μ_s and μ_d are static and dynamic friction coefficients, respectively, V_c is the characteristic velocity, namely the velocity at which half of the friction change has occurred, and γ represents the amount of slip velocity-induced weakening if $\gamma = 1 - (\mu_d/\mu_s)$ is positive, or strengthening if γ is negative.

When plastic yielding condition is locally reached we require a constant second invariant of deviatoric stresses (assuming the absence of elastic deformation)

$$\text{if } \sigma'_{II} = \sigma_{yield} : \left\{ \frac{D\sigma'_{II}}{Dt} = 0, \quad \varepsilon_{ij}^{elastic} = 0 \right\}; \quad (19)$$

then the stress components are similarly (i.e., isotropically) corrected so that

$$\sigma'_{ij} = \sigma'_{ij} \cdot \frac{\sigma_{yield}}{\sigma'_{II}}. \quad (20)$$

Accordingly, the local viscosity-like parameter η_{vp} decreases to weaken the material and to localise deformation:

$$\eta_{vp} = \eta \frac{\sigma'_{II}}{\eta\chi + \sigma'_{II}}, \quad (21)$$

where:

$$\chi = 2(\dot{\varepsilon}_{II} - \dot{\varepsilon}_{II}^{viscous}) = 2\left(\dot{\varepsilon}_{II} - \frac{1}{2\eta}\sigma'_{II}\right) \quad (22)$$

$$\dot{\varepsilon}_{II} = \sqrt{\dot{\varepsilon}_{xx}^2 + \dot{\varepsilon}_{xz}^2} . \quad (23)$$

Finally the visco-plastic viscosity η_{vp} is corrected during plastic deformation:

$$\eta_{vp} = \frac{\sigma_{yield}}{2\dot{\varepsilon}_{II}} . \quad (24)$$

On the other hand, if the plastic yielding condition is not satisfied, this means that the material is under elastic and/or viscous deformation (i.e., diffusion and/or dislocation creep), therefore

$$\eta_{vp} = \eta .$$

1.3. Eclogitization

Eclogitization of the continental mafic crust can have major effects on the evolution of continental plates. With the progression of the reaction, the eclogitized continental root becomes denser than the surrounding mantle and thus it is prone to foundering (Kay and Kay, 1993). Numerical models predict that high-density eclogite affects the orogeny evolution (Doin & Henry, 2001; Li et al., 2016) and, if sufficiently weak, can lead to delamination of the continental plate (Krystopowicz & Currie, 2013). Eclogitization of subducted crustal material is here implemented in a relatively simplified manner (Faccenda & Dal Zilio, 2017). More specifically, for the basalts of the upper and lower mafic crust, a phase transition from basalt to garnet-granulite and then eclogite (Ito & Kennedy, 1971) is applied. Eclogitization of the crust is implemented as a linear density increase with pressure and temperature from 0% to 16% in the P–T region between the experimentally determined garnet-in and plagioclase-out phase transitions in basalt (Ito & Kennedy, 1971). For temperatures lower than $T_{ecl_{min}} = 673\text{K}$ no eclogitization is possible. For temperatures between $T_{ecl_{min}}$ and $T_{ecl_{max}} = 873\text{K}$ the maximum density increase due to

eclogitization is linearly increasing with temperature from 0% to 16%.

1.4. Estimation of Moment Magnitude (M_W)

During the seismic cycle simulation we analyze all rupture events to determine their downdip rupture width (W). These events occurring throughout the orogen are recognized using a Rupture Detector Algorithm (RDA), which analyzes each Lagrangian marker in space and time throughout the simulation (Dal Zilio et al., 2018). If its velocity exceeds a threshold of $9.0 \times 10^{-9} \text{ m s}^{-1}$, while simultaneously stresses drop more than 0.4 MPa that marker's physical properties are stored in a synthetic data set. Subsequently markers are grouped into one event when they occur within 400 m of a marker that ruptured this or the previous time step. The rationale for choosing these thresholds comes from the minimally common stress drop (Allmann & Shearer, 2009) and our Eulerian grid size of 400 m, respectively.

From these spontaneous rupture paths we measure the rupture width (W) to estimate the moment magnitude (M_W) using the empirical scaling relations in Wells and Coppersmith (1994). This empirical relationship is available from regression analysis based on a large numbers of events in nature:

$$M_W = a + b \log(W), \quad (25)$$

where a and b are coefficients that vary with the style-of-faulting (i.e., normal or reverse faulting). We chose Wells and Coppersmith (1994) because they include various types of faulting and different tectonic environments.

1.5. Setup

The initial model domain consists of two continental plates separated by an oceanic basin (see Fig. 1a). The dimensions of the model box is $3000 \times 1200 \text{ km}^2$ (1921 x 347 nodes),

and all the mechanical boundaries are free slip. Variable grid spacing enables to reach a 400 m grid resolution in the central part of the domain where the continental collision takes place. Lithological structure are resolved with ~ 33 million markers. In order to study the interplay between subduction and orogenic evolution, we follow the semi-dynamic approach employed in Duretz et al. (2011). The initial conditions of the model are built during the initial stage of kinematic convergence. During this period, the oceanic subduction is kinematically prescribed using internal kinematic constrains (10 cm/yr until 200 km of shortening is accommodated). With ongoing convergence, the upper plate decouple from the lateral sides of the box; this zones accommodate hot mantle upwellings and are therefore the location where oceanic ridges spontaneously develop. After this model initialization step, the internal kinematic constrain is removed and the model is driven by internal, buoyancy forces. Thus, the obtained thermo-mechanical state is employed as the initial condition for a self-driven, retreating subduction and continental collision. The subduction and collision rates, which are not in steady state, are controlled by the contribution of slab pull, crustal buoyancy, and dissipative forces. We employ an additional 20 km thick layer of sticky air ($\eta_{air} = 10^{18}$ Pa s, $\rho_{air} = 1$ kg/m³) in order to mimic the effect of a free surface and enable the development of topography (Crameri et al., 2012).

The thermal structure of the oceanic lithosphere was calculated from the half space cooling model for a given plate age (Turcotte & Schubert, 2002) using a slab age of 70 Ma and a diffusivity of 10^{-6} m² s⁻¹. The initial continental geotherm is defined as a linear temperature variation from the model surface (T=293 K) to the lithosphere–asthenosphere boundary (T=1617.6 K), the left and right sides of the model domain are insulating boundaries. The geothermal gradient in the asthenospheric mantle below the lithosphere is 0.5 K/km (Fig. 1c).

In order to initiate subduction a weak zone was imposed on the right ocean–upper plate transition. The weak zone cuts through the whole lithospheric mantle with an angle of $\sim 30^\circ$ and is

characterized by weak plastic strength (1 MPa) and wet olivine rheology (Ranalli, 1995). Despite the fact that subduction initiation can be modelled in a geologically more relevant manner (Nikolaeva et al., 2010), the use of such a weak zone remains useful for our specific setup.

<i>Material</i>	ρ_0^b	E_a^a	V_a^a	n^a	η_0^a	$Hr^{b,c}$	k^a	G	$\mu_s^{d,e,f}$	$\lambda^{g,h}$
<i>flow law</i> ^a	($kg\ m^{-3}$)	($kJ\ mol^{-1}$)	(J/bar)		($Pa^n\ s$)	(μWm^{-3})	$Wm^{-1}K^{-1}$	(GPa)		
Sediments (Wet Qz)	2600	154	1.2	2.3	1.97×10^{17}	1.5	$[0.64 + 807/(T + 77)]$ $exp(4 \cdot 10^{-6}P)$	25	0.35	0.6
Upper cont. crust (Wet Qz)	2750	154	0.8	2.3	1.97×10^{17}	0.25	$[0.64 + 807/(T + 77)]$ $exp(4 \cdot 10^{-6}P)$	34	0.6	0.6
Lower cont. crust (Mafic Granulite)	3000	445	0.8	4.2	1.25×10^{21}	1.5	$[0.64 + 807/(T + 77)]$ $exp(4 \cdot 10^{-6}P)$	34	0.6	0.6
Upper oc. crust (Wet Qz)	3000	154	0.8	2.3	1.97×10^{17}	0.25	$[1.18 + 974/(T + 77)]$ $exp(4 \cdot 10^{-6}P)$	38	0.6	0.95
Lower oc. crust (Plg-An 75%)	3300	238	0.8	3.2	4.8×10^{22}	0.0022	$[1.18 + 974/(T + 77)]$ $exp(4 \cdot 10^{-6}P)$	38	0.6	0.6
Mantle (Dry Olivine)	3300	532	0.8	3.5	3.98×10^{16}	0.0022	$[0.73 + 1293/(T + 77)]$ $exp(4 \cdot 10^{-6}P)$	67	0.6	0.6

Table S1: Rheological parameters. ρ_0 is the reference density, E_a is the activation energy, V_a is the activation volume, n is the stress exponent, η_0 is the reference viscosity, Hr is the radiogenic heat production, G is the shear modulus, μ_s is the static friction coefficient and λ is the pore-fluid pressure factor (P_{fluid}/P_{solid}). Other properties for all rock types: cohesion (C) is 1 MPa (Schultz, 1995), specific heat capacity (C_p) is $1000\ J\ kg^{-1}K^{-1}$, thermal conductivity (k) is in $Wm^{-1}K^{-1}$ at T_K and P_{MPa} , thermal expansion $\alpha_\rho = 3 \times 10^{-5}\ K^{-1}$ and compressibility $\beta_\rho = 1 \times 10^{-3}\ MPa^{-1}$. ^a Ranalli (1995); ^b Turcotte and Schubert (2002); ^c Rudnick and Fountain (1995); ^d Di Toro et al. (2011); ^e Del Gaudio et al. (2009); ^f Den Hartog et al. (2012); ^g Sibson (1994); ^h Seno (2009).

<i>Model</i>	Plate age (My)	Density contrast (kg/m^3)	Depth slab breakoff (km)	Slab Rollback Orogeny
<i>SRO-T1</i>	40	39.9	125	no
<i>SRO-T2</i>	50	48.5	171	no
<i>SRO-T3</i>	60	57.3	203	no
<i>SRO-T4</i> *	70	64.1	245	yes
<i>SRO-T5</i>	80	70.1	301	yes
<i>SRO-T6</i>	90	74.5	352	yes
<i>SRO-T7</i>	100	77.5	380	yes

* *Reference model*

Table S2: Parameters of the selected models.

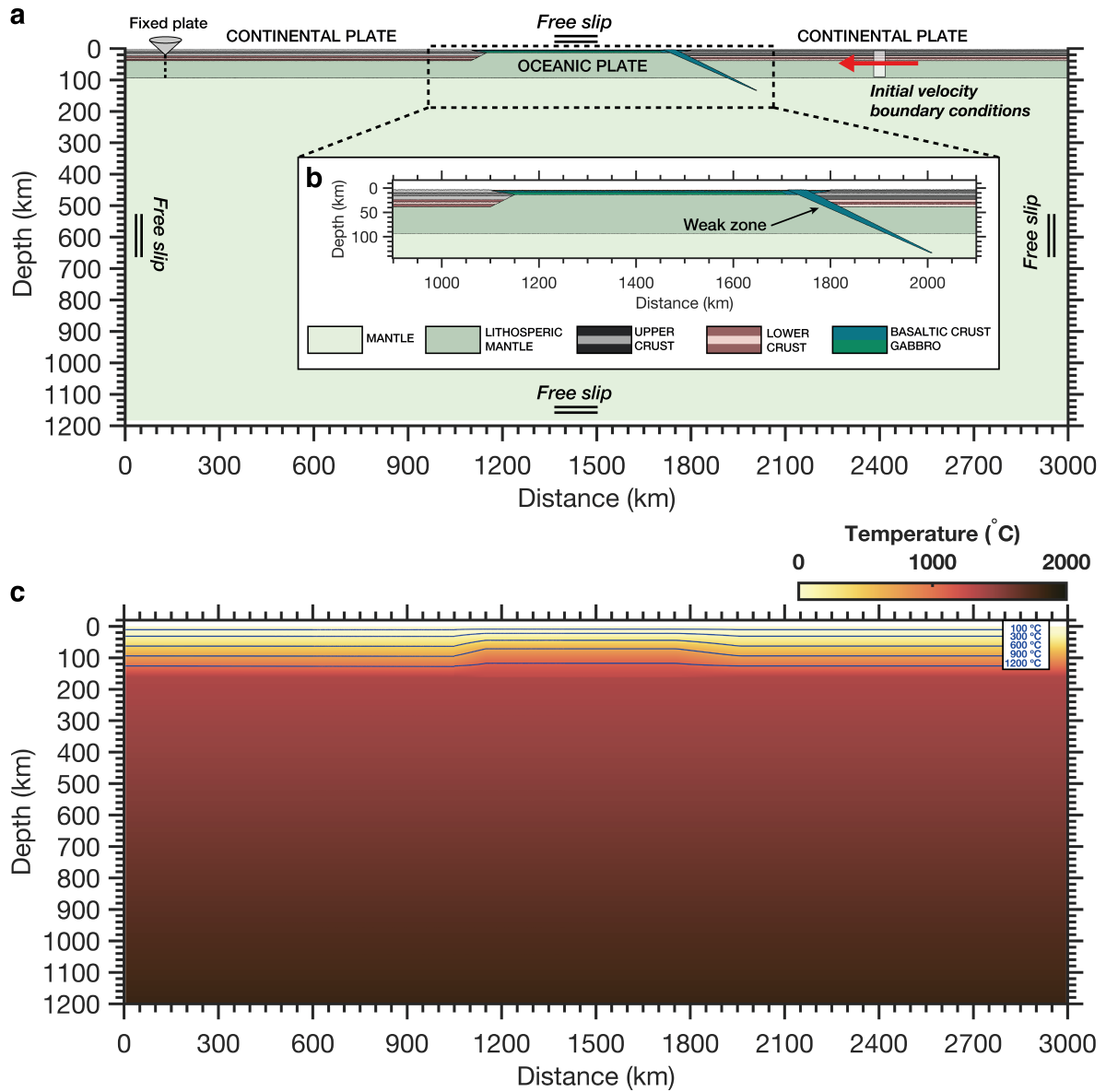


Figure S1: 2-D initial setup. **a**, Initial composition map including boundary conditions. **b**, Zoom of oceanic plate and pre-imposed weak zone to initiate subduction. The model simulates subduction initiation through the use of a fixed convergence rate on the upper plate until ~200 km of oceanic crust has been subducted. Plate convergence rate is applied at 2500 km on the right (upper) plate (red arrow). **c**, Initial temperature distribution.

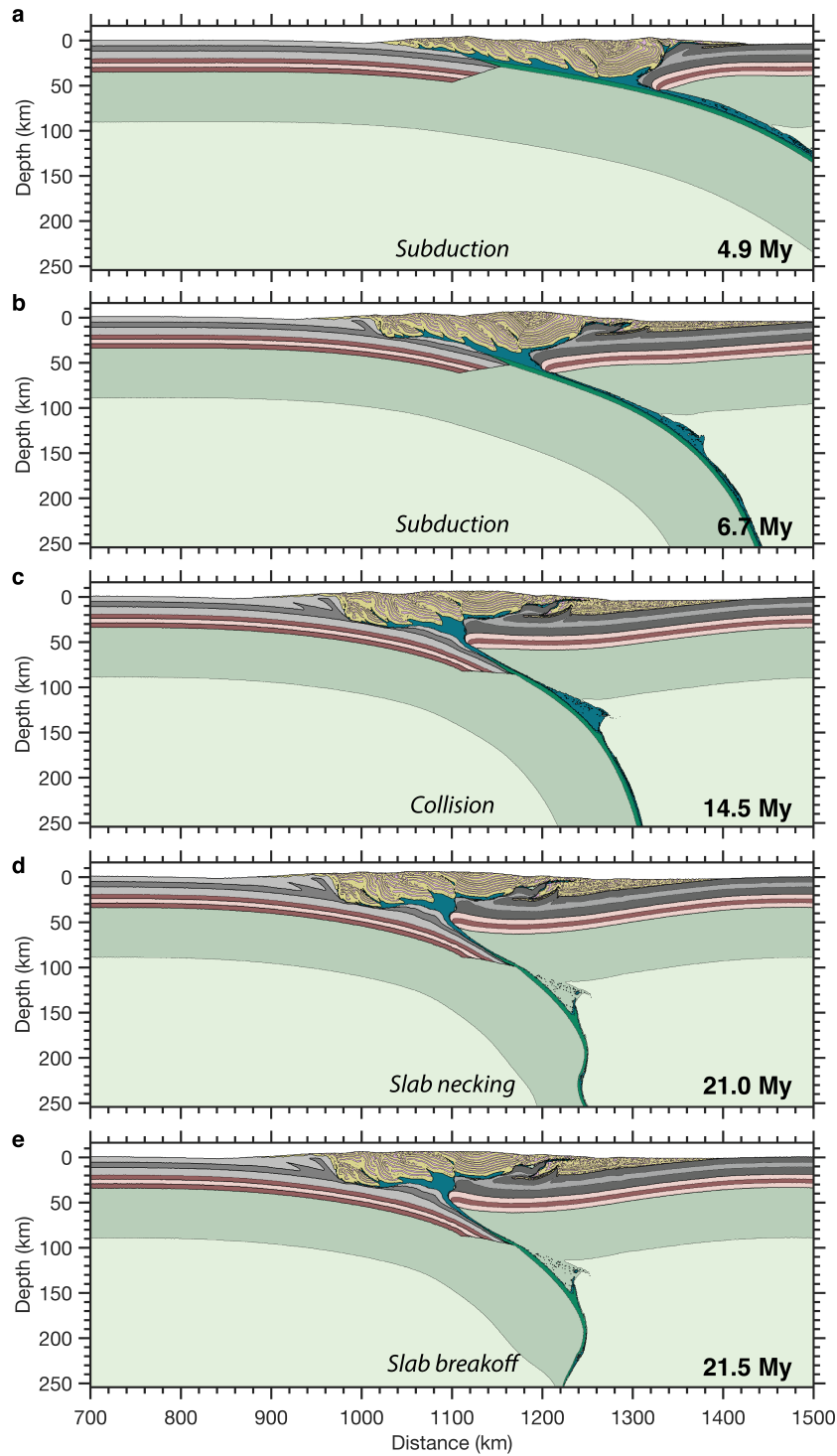


Figure S2: Long-term evolution of subduction (a–b), collision (c), slab necking (d), and slab breakoff (e). The early phases of the models consist of oceanic plate consumption and ocean closure. The collisional regime is greatly affected by the buoyant and rheologically weak materials entering the subduction channel from above. The final structure is that of a *coupled* collision system.

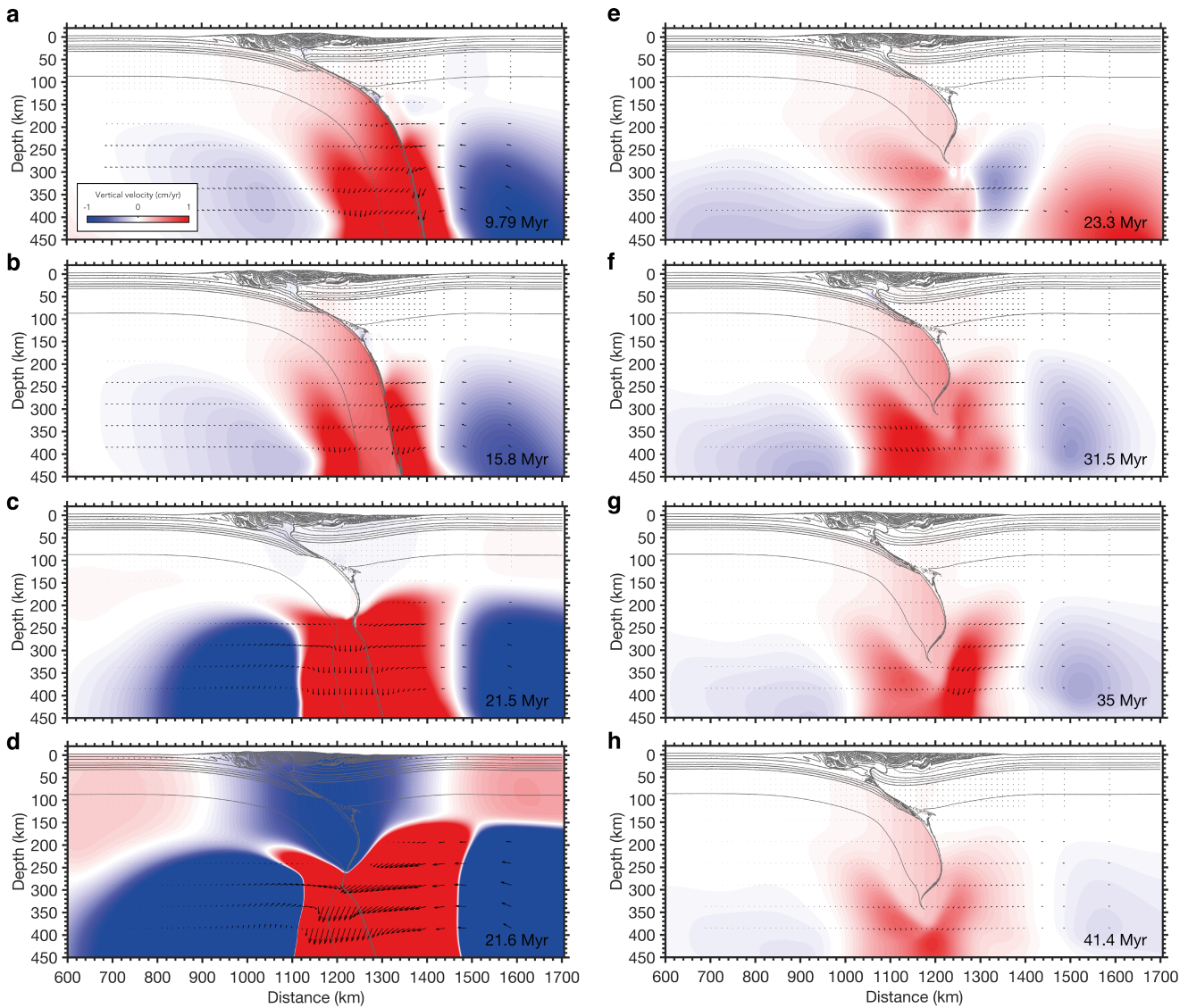


Figure S3: Vertical velocity of the reference model (model SRO-T4 – Table S2) at different stages. (a,b) Convergence stops slows down after both continental plates meet. Prolonged slab steepening initiates plate decoupling and slab retreat, triggering exhumation of the crust in a buoyant flow manner. (c,d) Detachment occurs approximately 10 My after the termination of subduction. As soon as breakoff ends, the orogen undergoes a short period of extension (Fig. S3), coeval with extrusion of the buoyant continental crust. (e-h) After slab breakoff, slow yet persistent sinking and bending of the remaining slab results in the migration of the whole orogen towards the foreland basin. The velocity field shows how the vertical sinking of the post breakoff remaining slab translates into horizontal convergence of the upper plate and uplift in the core of the orogen (Fig. 4c).

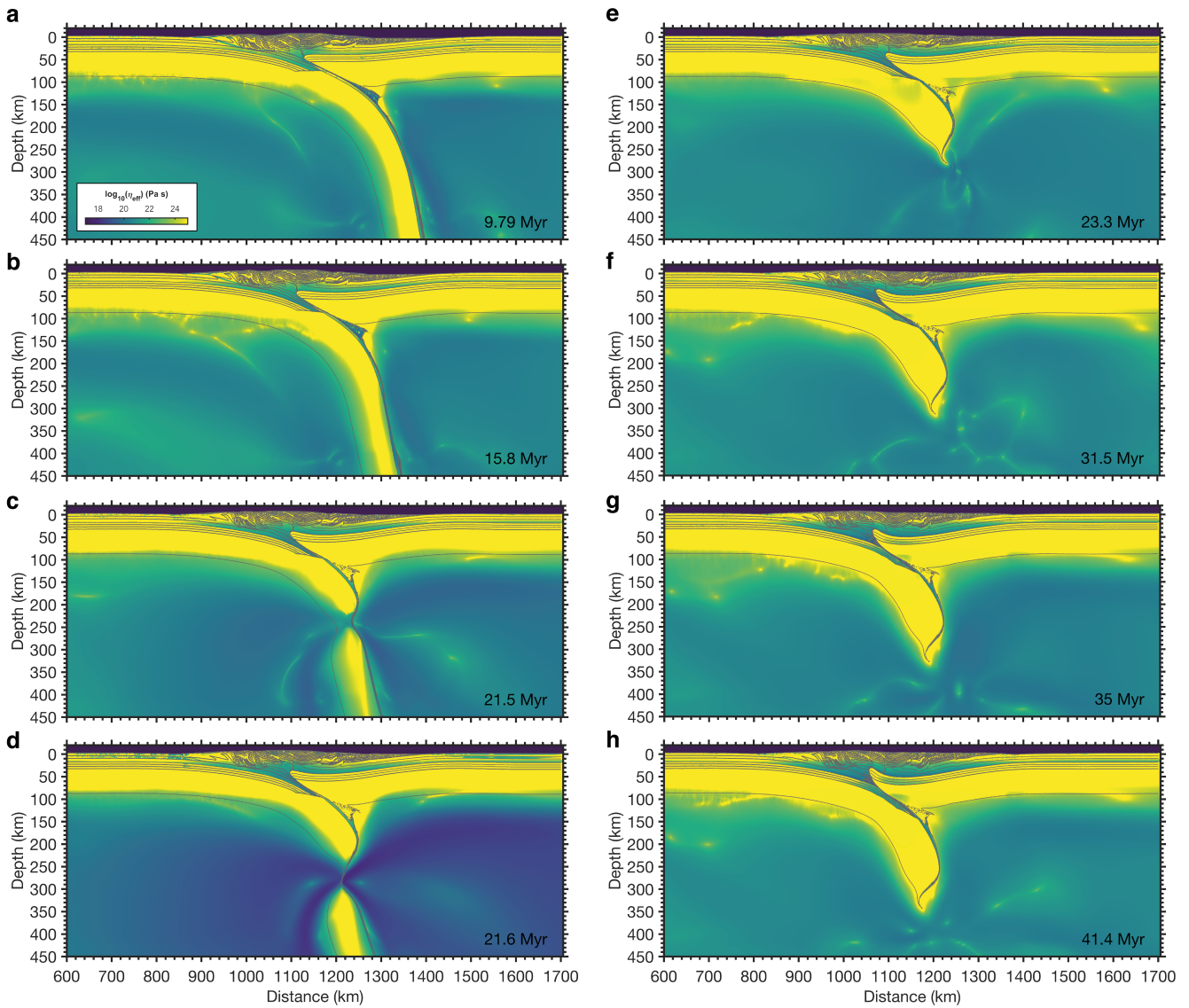


Figure S4: Viscosity field of the reference model (model **SRO-T4** – Table S2) at different stages. **(a,b)** Syn-collisional dynamics. **(c,d)** Slab detachment occurs at a depth of ~ 240 km during the stage of slab steepening. Slab necking is due to the combined action of viscous creep in the hotter crust and mantle and Peierls mechanism in the cold mantle lithosphere of the slab core. **(e-h)** The viscosity contrast in the orogen (between the deeper crust and the brittle high strength shallow crust), illustrates how the long-term tectonic evolution, temperature, and crustal properties affect the architecture of the orogen and thereby their short-term spatial distribution of seismicity shown in Fig. 3b.

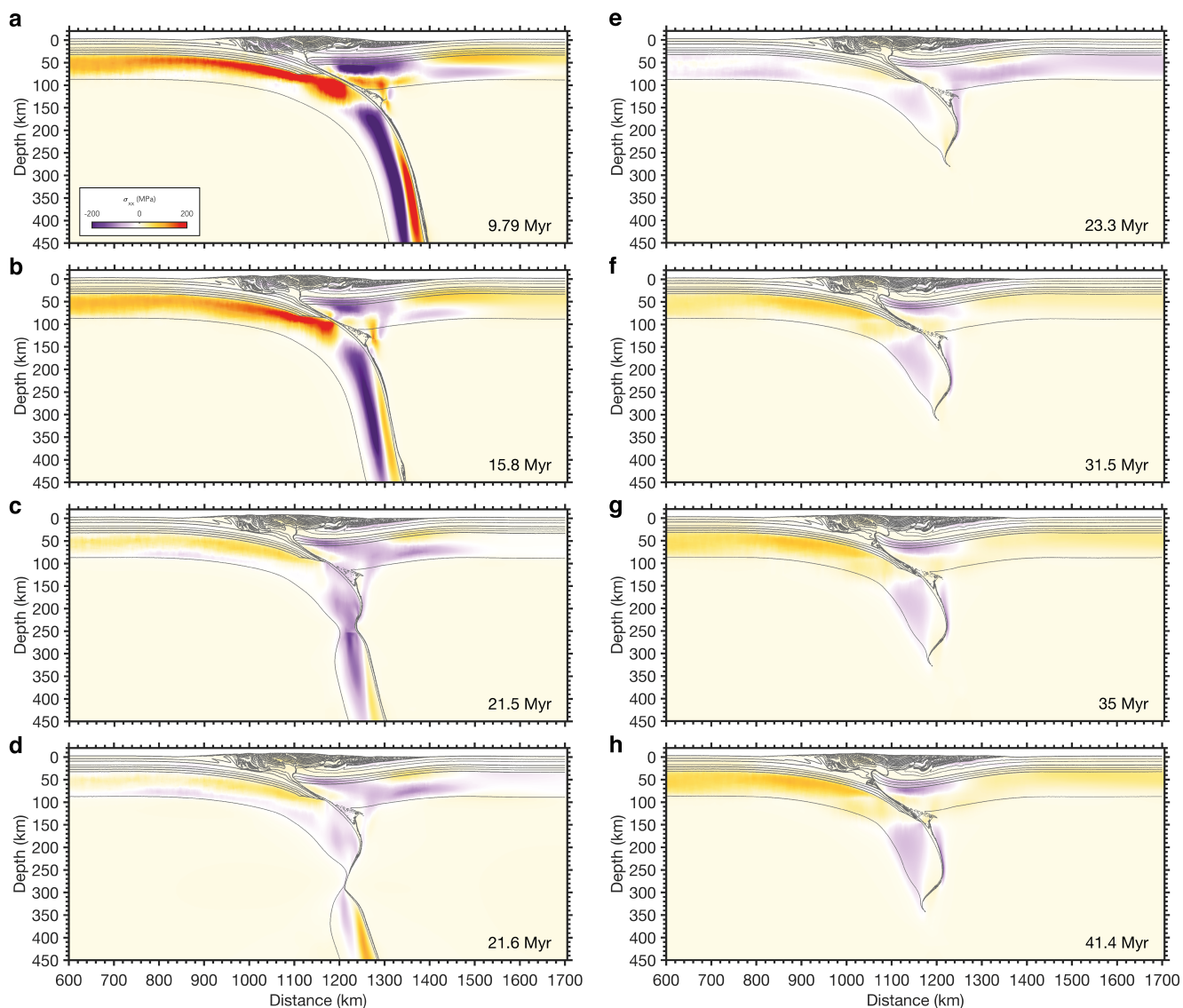


Figure S5: Stress field of the reference model (model SRO-T4 – Table S2) at different stages through time. (a,b) Syn-collisional dynamics and deceleration of the convergence rate. (c,d) Slab detachment occurs at a depth of ~ 240 km during the stage of slab steepening. (e) After slab breakoff, stresses are significantly reduced. (f-h) The negative buoyancy provided by the remaining slab induces slab retreat, which results in bending-related extensional stresses in the lower plate and suction force across the plate interface and on the upper plate.

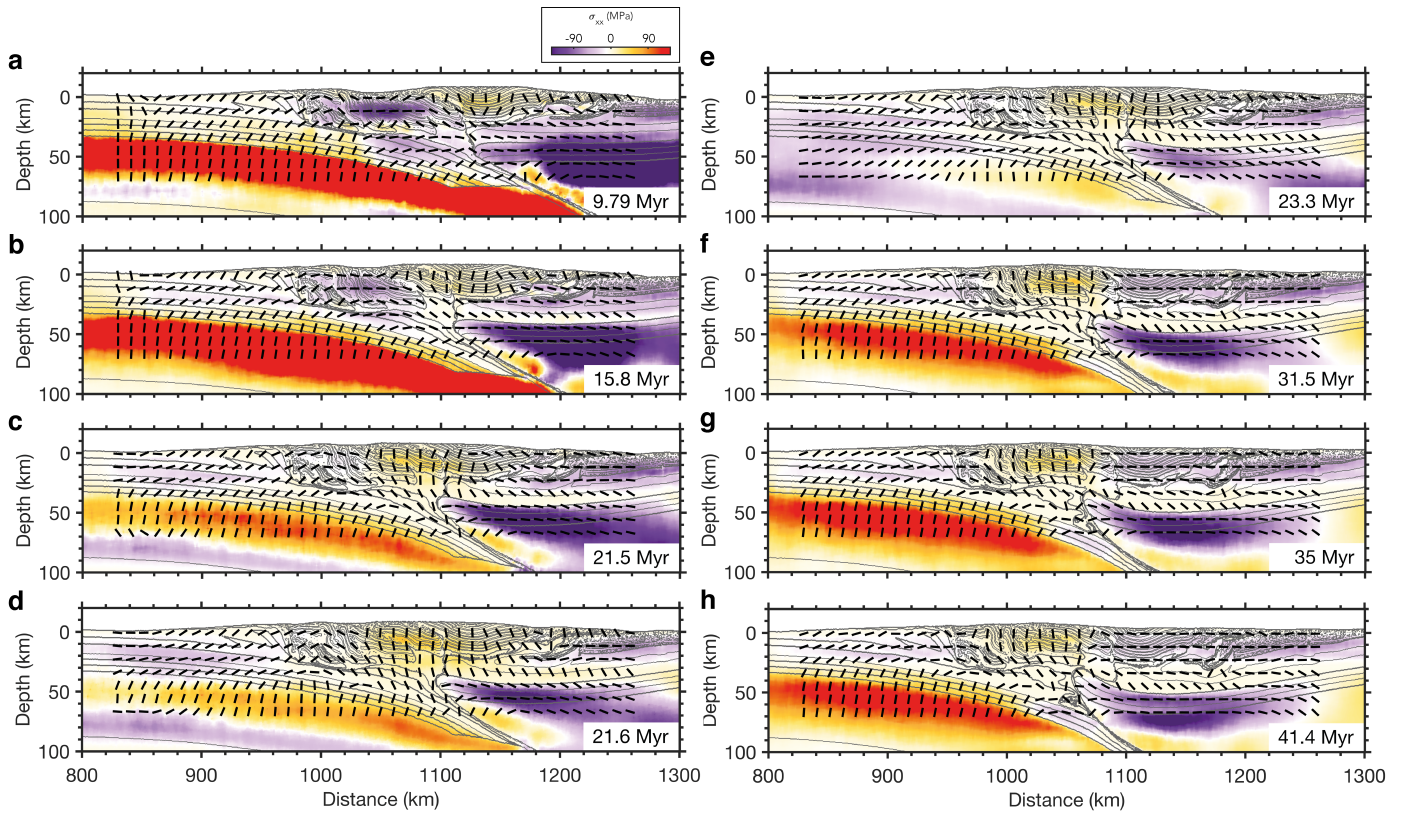


Figure S6: Zoom of stress field of the reference model (model **SRO-T4** – Table S2) at different stages. **(a,b)** Syn-collisional dynamics, **(c,d)** slab detachment, and **(e-h)** post-collisional evolution.

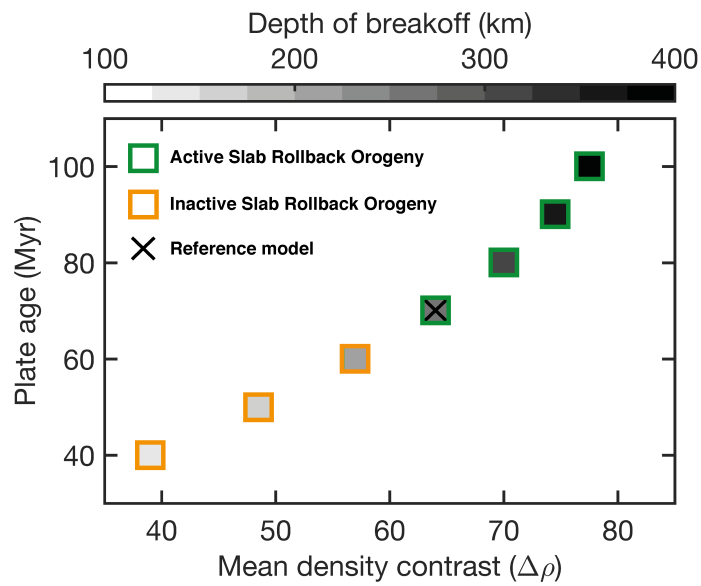


Figure S7: Sensitivity to the choice of different plate's age. The older the plate, the larger the density contrast, and the deeper the slab breakoff. This means that the Slab Rollback Orography model can be activated only when the length of the remaining slab (and its negative buoyancy) is long enough (age ≥ 70 My; green markers). Black cross indicates the reference model **SRO-T4** (see Table S2).

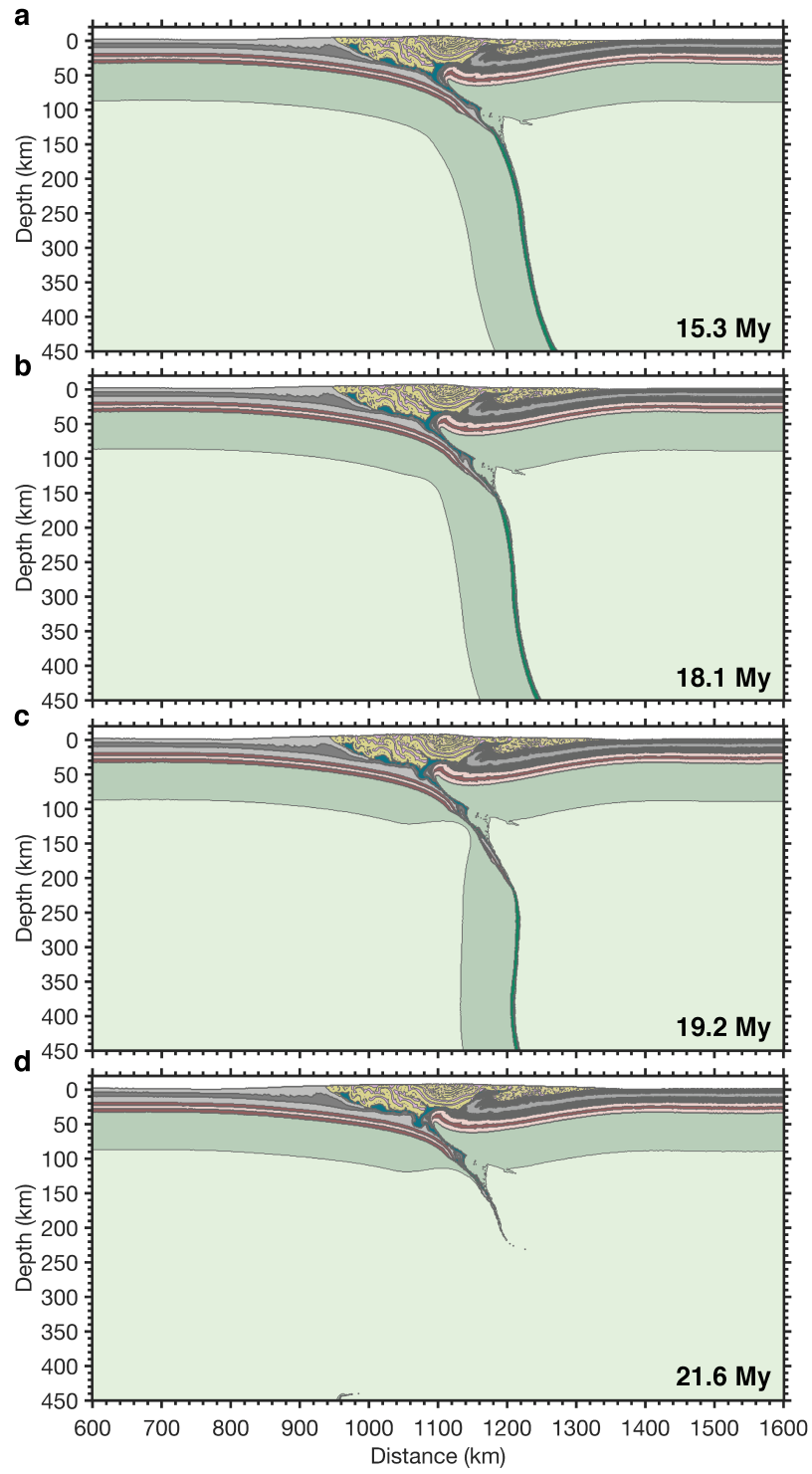


Figure S8: Temporal evolution of model SRO-T1 (see Table S2).

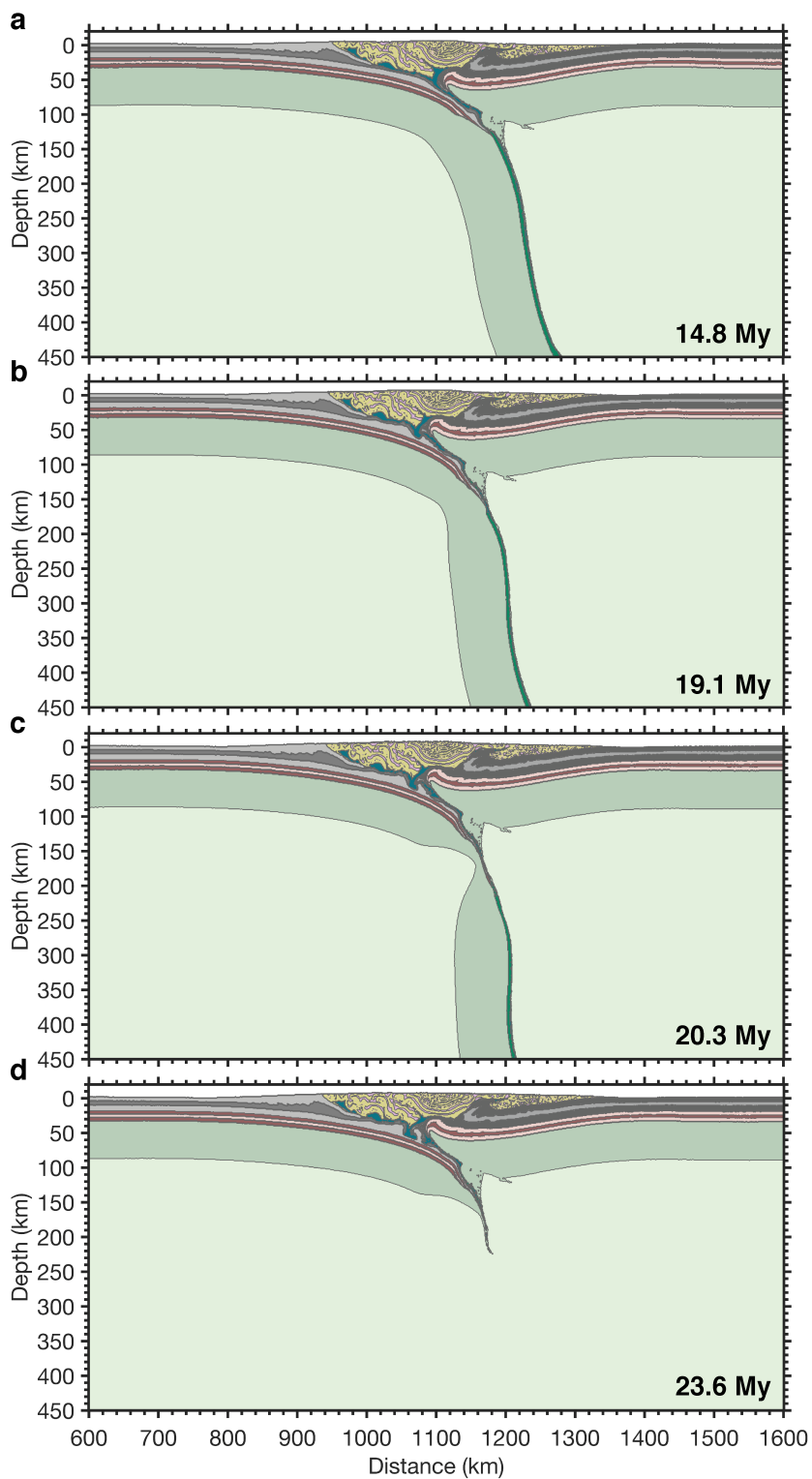


Figure S9: Temporal evolution of model SRO-T2 (see Table S2).

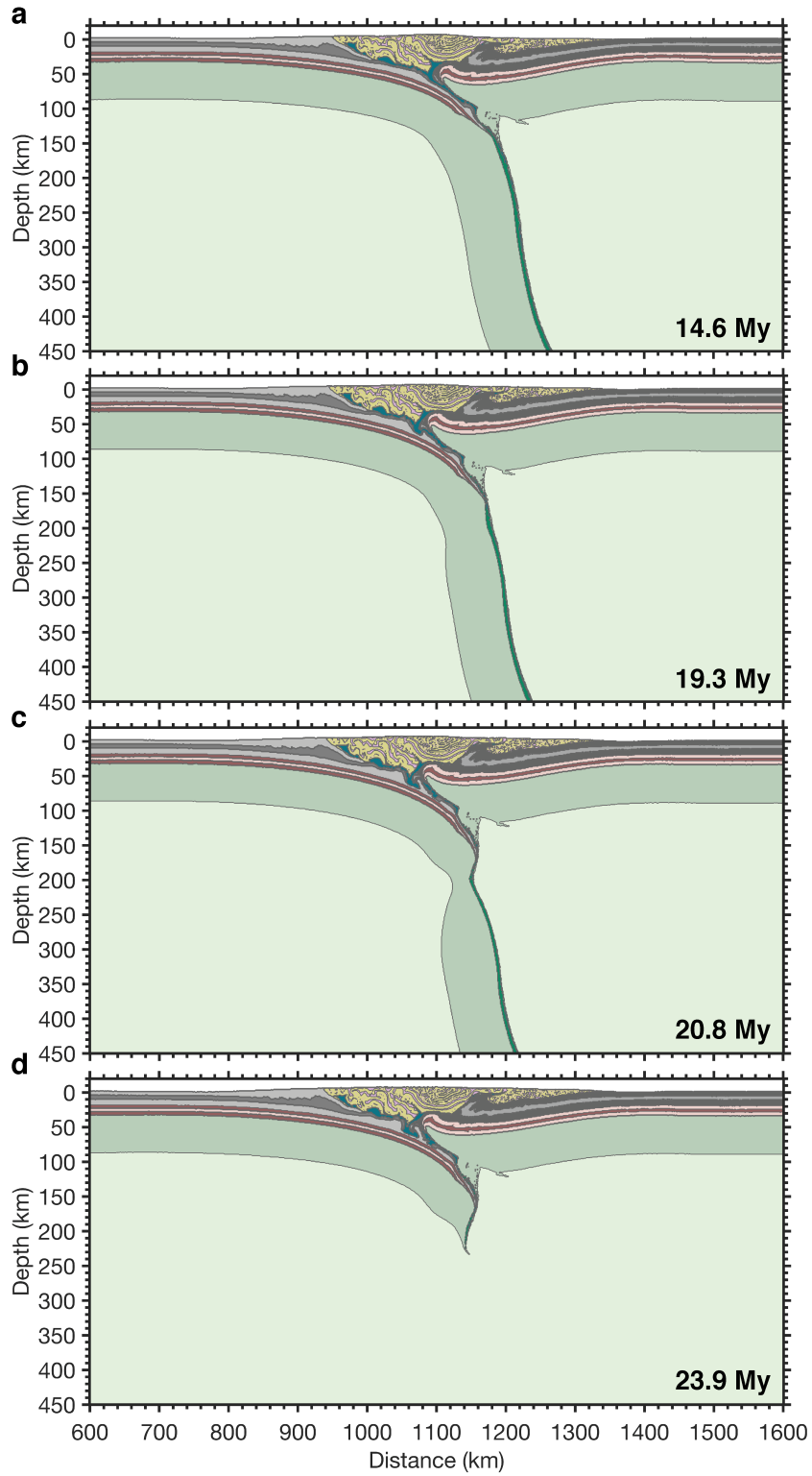


Figure S10: Temporal evolution of model SRO-T3 (see Table S2).

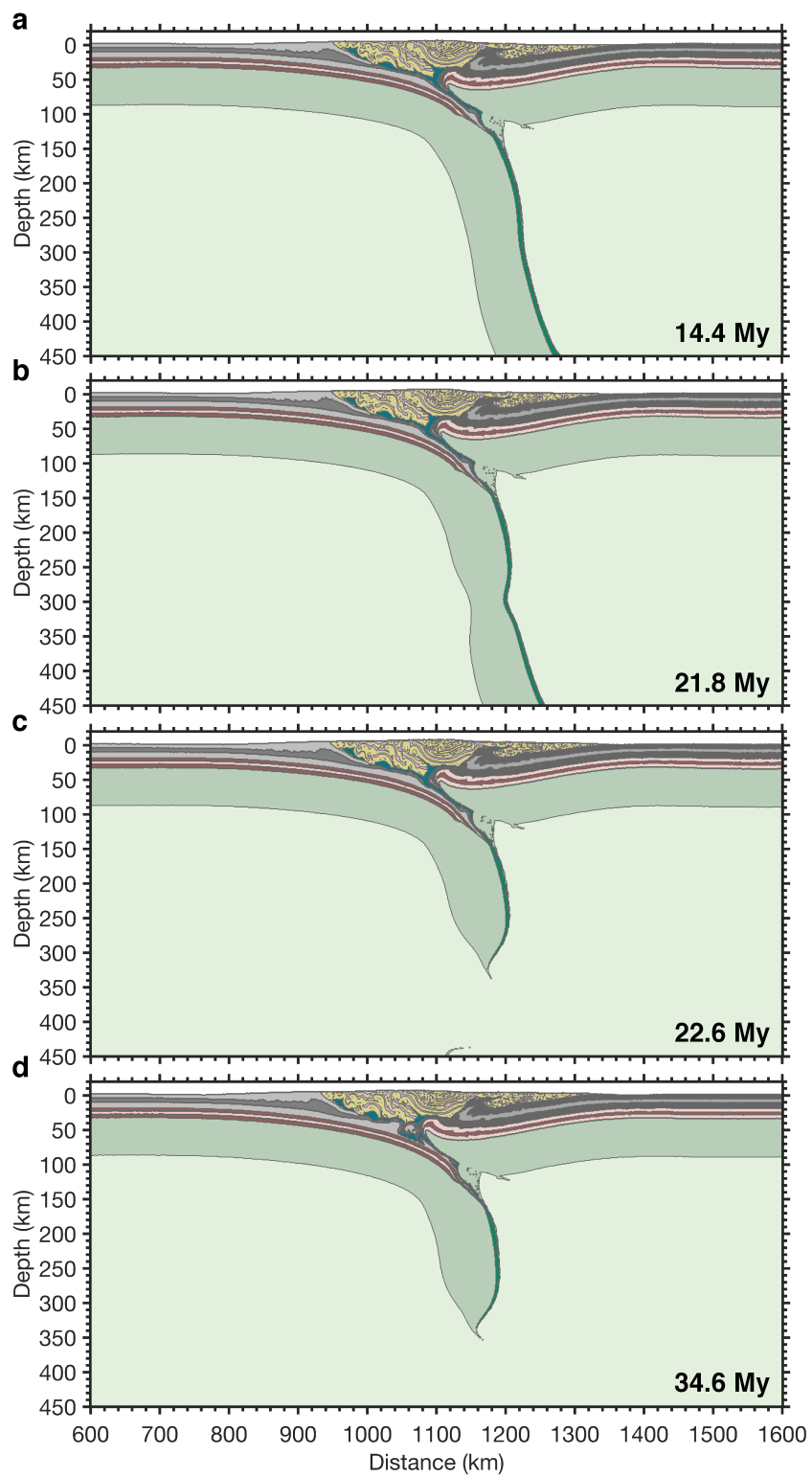


Figure S11: Temporal evolution of model SRO-T5 (see Table S2).

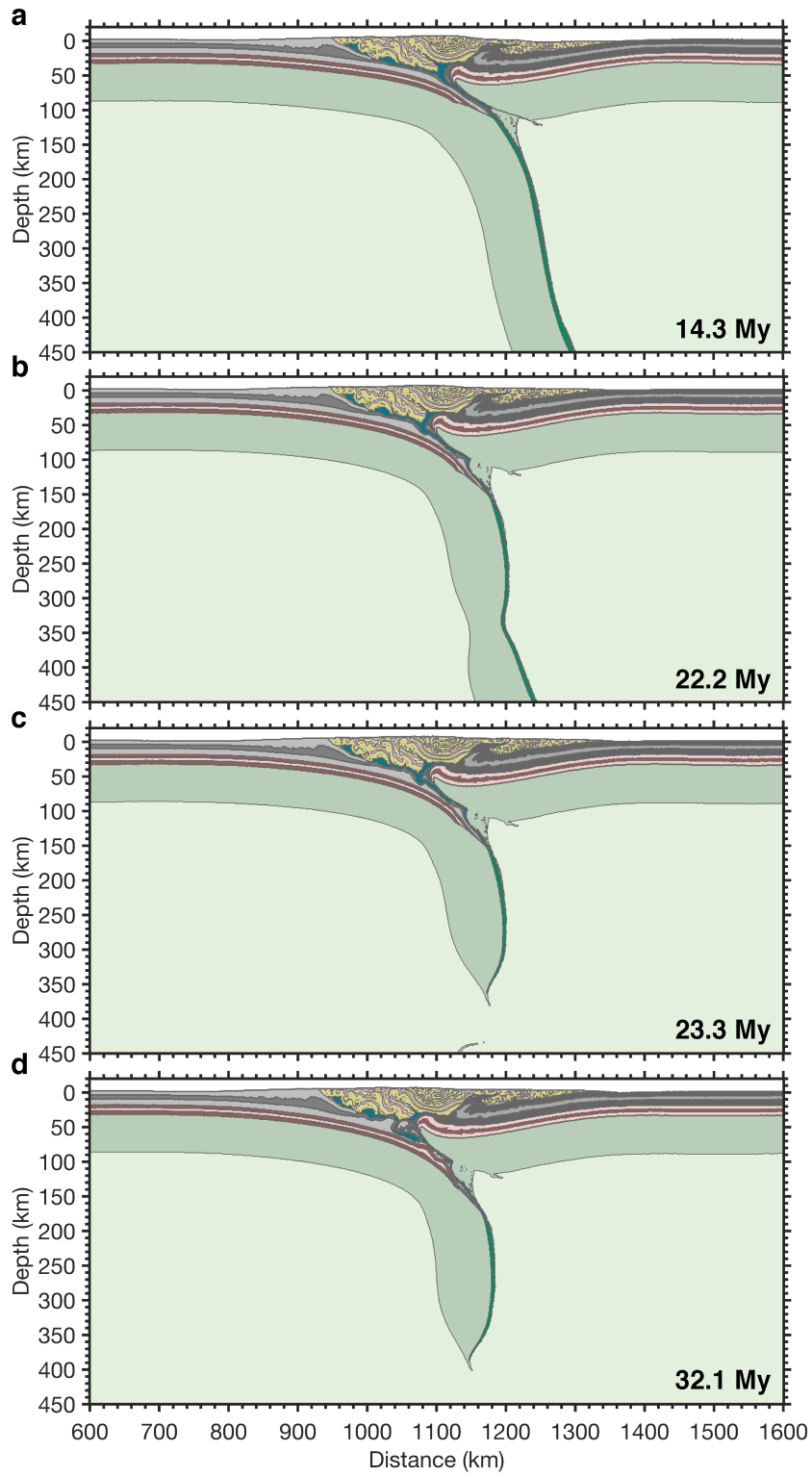


Figure S12: Temporal evolution of model SRO-T6 (see Table S2).

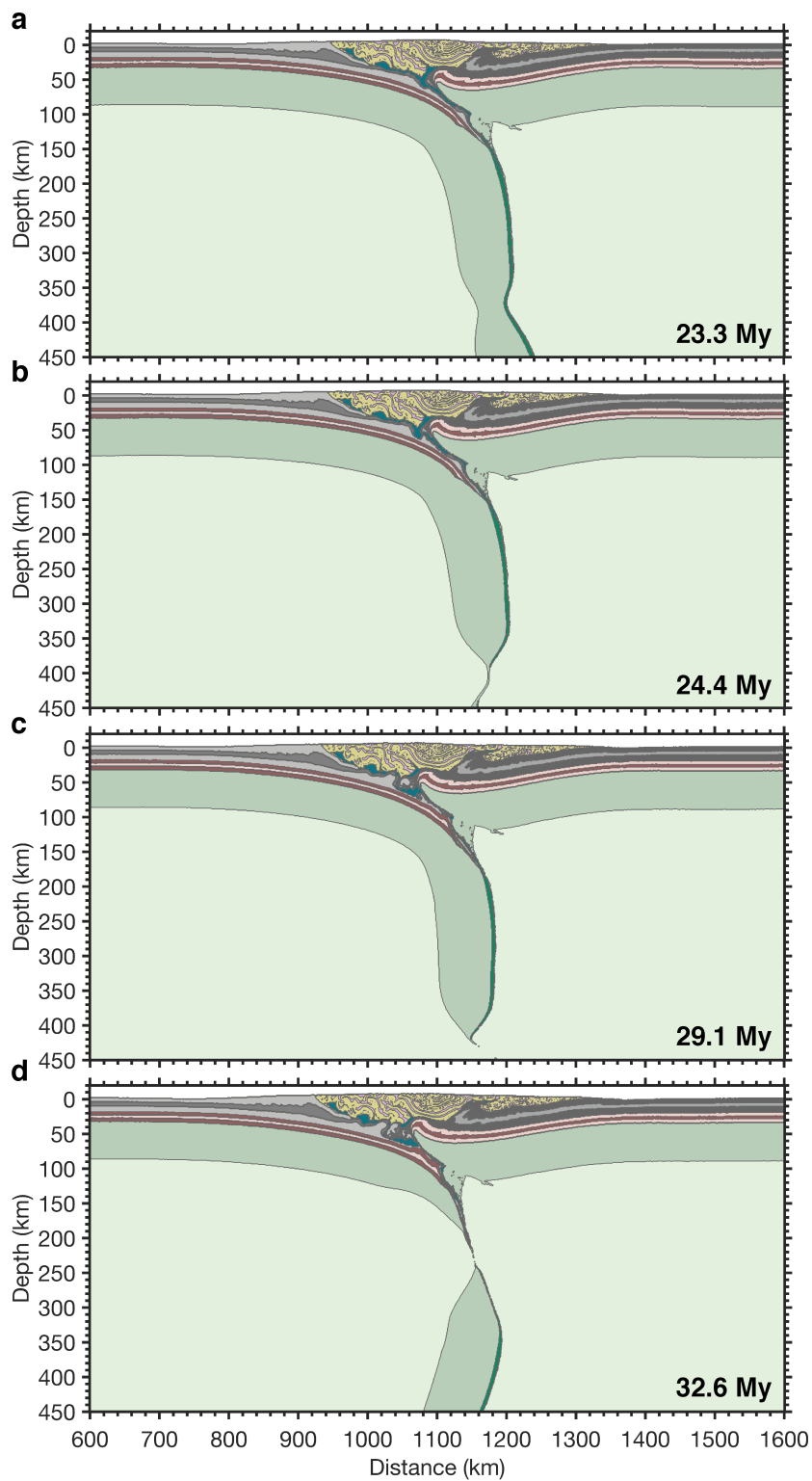


Figure S13: Temporal evolution of model **SRO-T7** (see Table S2).

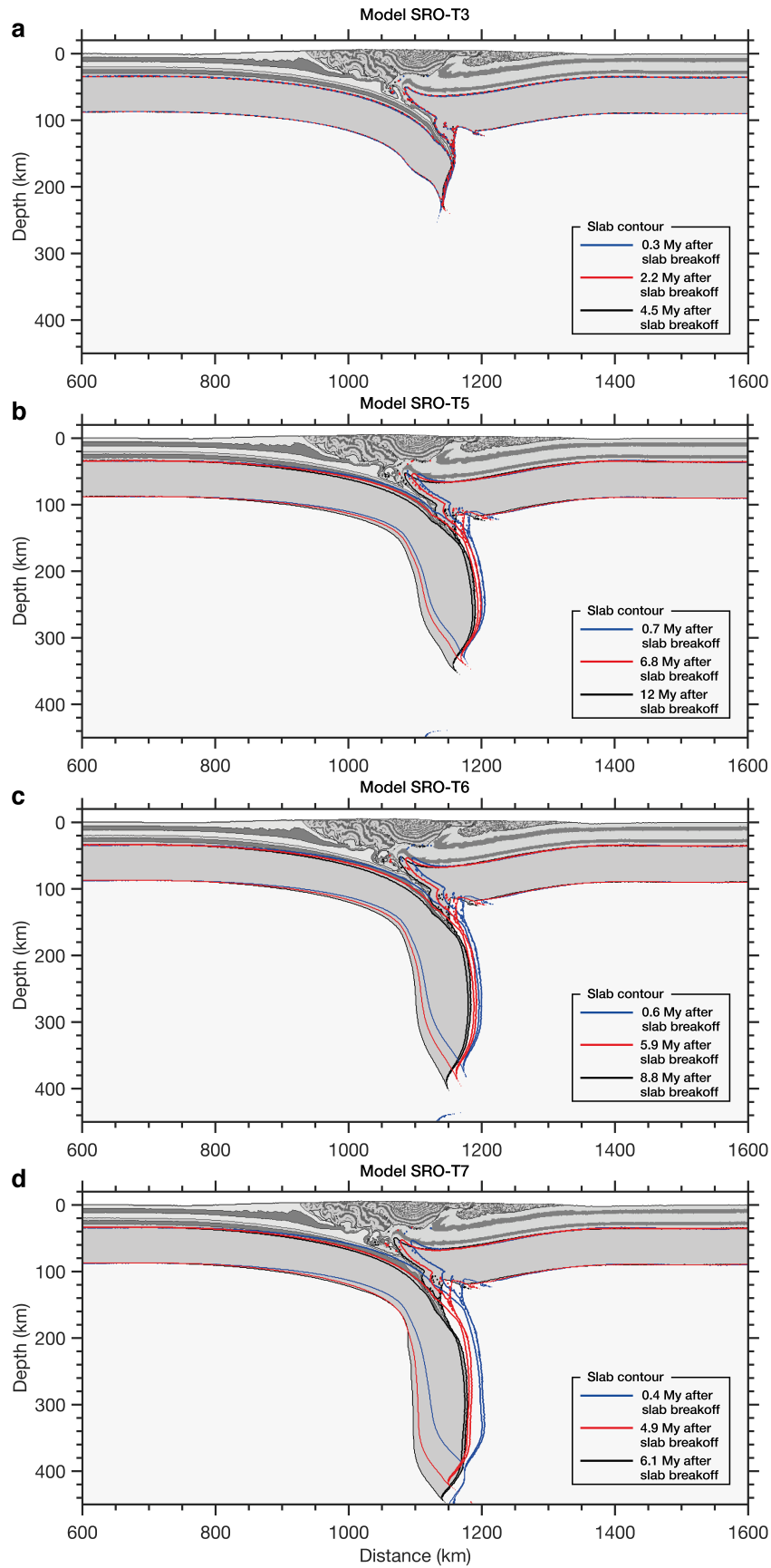


Figure S14: Post-collisional evolution for models **SRO T3**, **T5**, **T6**, and **T7** (Table S2), including superimposed contours of the slab geometries. Composition (gray scale map) shows the final structure. While model **SRO-T3** is characterized by a shallow slab breakoff, which does not result in a post-collisional slab retreat, models **SRO T5**, **T6**, and **T7** show slab retreat and steepening of the post-breakoff residual slab.

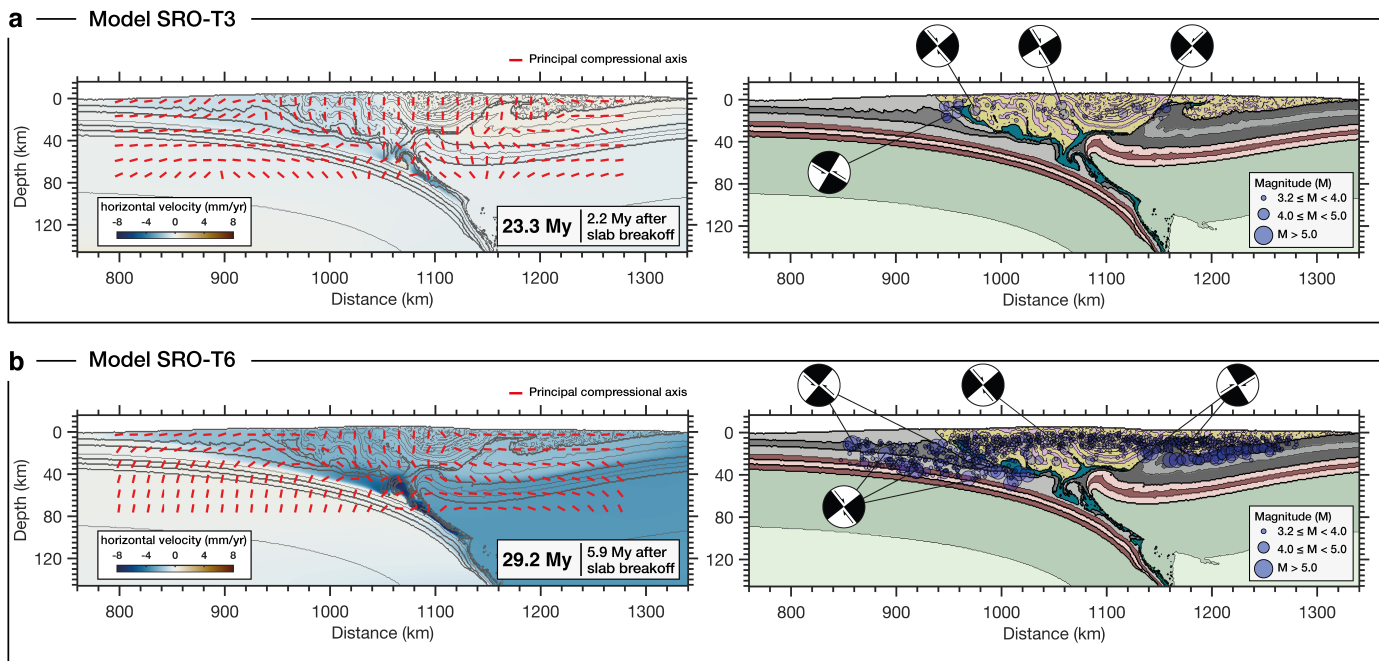


Figure S15: Horizontal velocity, orientation of maximum (compression) principal stresses, and short-term seismicity pattern for models (a) SRO-T3 and (b) SRO-T6 (Table S2). The inferred stress axes show a broad pattern of different tectonic regimes throughout the orogen. Cluster of seismicity and the inferred 2-D focal mechanisms display different style of faulting. Model SRO-T3 is not characterized by a post-collisional retreat of the residual slab. As a result, the general pattern of seismicity displays only a few events in the core of the orogen. On the other hand, the post-collisional retreat in model SRO-T6 results in a broad cluster of seismic events, which are controlled by slab dynamics and related mantle flow.

Movie S1: Long-term evolution of the reference model, including oceanic subduction, continent-continent collision, slab necking, slab breakoff, and post-collisional evolution. Time is incremented from the start of the experiment.

Supporting References

- Allmann, B. P., & Shearer, P. M. (2009). Global variations of stress drop for moderate to large earthquakes. *Journal of Geophysical Research: Solid Earth*, *114*(B1).
- Ampuero, J.-P., & Ben-Zion, Y. (2008). Cracks, pulses and macroscopic asymmetry of dynamic rupture on a bimaterial interface with velocity-weakening friction. *Geophysical Journal International*, *173*(2), 674–692.
- Crameri, F., Schmeling, H., Golabek, G., Duretz, T., Orendt, R., Buitter, S., . . . Tackley, P. (2012). A comparison of numerical surface topography calculations in geodynamic modelling: An evaluation of the ‘sticky air’ method. *Geophysical Journal International*, *189*(1), 38–54.
- Dal Zilio, L., van Dinther, Y., Gerya, T. V., & Pranger, C. C. (2018, 1). Seismic behaviour of mountain belts controlled by plate convergence rate. *Earth and Planetary Science Letters*, *482*, 81–92.
- Del Gaudio, P., Di Toro, G., Han, R., Hirose, T., Nielsen, S., Shimamoto, T., & Cavallo, A. (2009). Frictional melting of peridotite and seismic slip. *Journal of Geophysical Research: Solid Earth*, *114*(B6).
- Den Hartog, S., Niemeijer, A., & Spiers, C. (2012). New constraints on megathrust slip stability under subduction zone p–t conditions. *Earth and Planetary Science Letters*, *353*, 240–252.
- Di Toro, G., Han, R., Hirose, T., De Paola, N., Nielsen, S., Mizoguchi, K., . . . Shimamoto, T. (2011). Fault lubrication during earthquakes. *Nature*, *471*(7339), 494–498.
- Doin, M.-P., & Henry, P. (2001). Subduction initiation and continental crust recycling: the roles of rheology and eclogitization. *Tectonophysics*, *342*(1-2), 163–191.
- Duretz, T., Gerya, T. V., & May, D. A. (2011). Numerical modelling of spontaneous slab breakoff and subsequent topographic response. *Tectonophysics*, *502*(1-2), 244–256.
- Evans, B., & Goetze, C. (1979). The temperature variation of hardness of olivine and its implication for polycrystalline yield stress. *Journal of Geophysical Research: Solid Earth*, *84*(B10), 5505–5524.

- Faccenda, M., & Dal Zilio, L. (2017). The role of solid–solid phase transitions in mantle convection. *Lithos*, 268, 198–224.
- Gerya, T. (2010). *Introduction to numerical geodynamic modelling*. Cambridge University Press.
- Gerya, T., & Yuen, D. (2007). Robust characteristics method for modelling multiphase visco-elasto-plastic thermo-mechanical problems. *Physics of the Earth and Planetary Interiors*, 163(1), 83–105.
- Ito, K., & Kennedy, G. C. (1971). An experimental study of the basalt-garnet granulite-eclogite transition. *The structure and physical properties of the Earth's crust*, 14, 303–314.
- Kameyama, M., Yuen, D. A., & Karato, S.-I. (1999). Thermal-mechanical effects of low-temperature plasticity (the peierls mechanism) on the deformation of a viscoelastic shear zone. *Earth and Planetary Science Letters*, 168(1-2), 159–172.
- Karato, S.-i., Riedel, M. R., & Yuen, D. A. (2001). Rheological structure and deformation of subducted slabs in the mantle transition zone: implications for mantle circulation and deep earthquakes. *Physics of the Earth and Planetary Interiors*, 127(1-4), 83–108.
- Katayama, I., & Karato, S.-i. (2008). Low-temperature, high-stress deformation of olivine under water-saturated conditions. *Physics of the Earth and Planetary Interiors*, 168(3), 125–133.
- Krystopowicz, N. J., & Currie, C. A. (2013). Crustal eclogitization and lithosphere delamination in orogens. *Earth and Planetary Science Letters*, 361, 195–207.
- Li, Z.-H., Liu, M., & Gerya, T. (2016). Lithosphere delamination in continental collisional orogens: A systematic numerical study. *Journal of Geophysical Research: Solid Earth*, 121(7), 5186–5211.
- Lu, G., Kaus, B. J., & Zhao, L. (2011). Thermal localization as a potential mechanism to rift cratons. *Physics of the Earth and Planetary Interiors*, 186(3-4), 125–137.
- Nikolaeva, K., Gerya, T., & Marques, F. (2010). Subduction initiation at passive margins: Numerical modeling. *Journal of Geophysical Research: Solid Earth (1978–2012)*, 115(B3).

- Prager, W., & Drucker, D. (1952). Soil mechanics and plastic analysis or limit design, 0. *Appi. Math*, 10(2), 157–165.
- Ranalli, G. (1995). *Rheology of the earth*. Springer.
- Rudnick, R. L., & Fountain, D. M. (1995). Nature and composition of the continental crust: a lower crustal perspective. *Reviews of geophysics*, 33(3), 267–309.
- Schultz, R. (1995). Limits on strength and deformation properties of jointed basaltic rock masses. *Rock Mechanics and Rock Engineering*, 28(1), 1–15.
- Seno, T. (2009). Determination of the pore fluid pressure ratio at seismogenic megathrusts in subduction zones: Implications for strength of asperities and andean-type mountain building. *Journal of Geophysical Research: Solid Earth*, 114(B5).
- Sibson, R. H. (1994). Crustal stress, faulting and fluid flow. *Geological Society, London, Special Publications*, 78(1), 69–84. Retrieved from <http://sp.lyellcollection.org/content/78/1/69> doi: 10.1144/GSL.SP.1994.078.01.07
- Turcotte, D., & Schubert, G. (2002). *Geodynamics*. Cambridge University Press.
- van Dinther, Y., Gerya, T., Dalguer, L., Mai, P. M., Morra, G., & Giardini, D. (2013). The seismic cycle at subduction thrusts: Insights from seismo-thermo-mechanical models. *Journal of Geophysical Research: Solid Earth*, 118(12), 6183–6202.
- Van Heck, H., & Tackley, P. (2008). Planforms of self-consistently generated plates in 3d spherical geometry. *Geophysical Research Letters*, 35(19).
- Wells, D. L., & Coppersmith, K. J. (1994). New empirical relationships among magnitude, rupture length, rupture width, rupture area, and surface displacement. *Bulletin of the seismological Society of America*, 84(4), 974–1002.